RSC Advances

PAPER

Check for updates

Cite this: *RSC Adv.*, 2018, **8**, 15427

Electroless plating of a Sn–Ni/graphite sheet composite with improved cyclability as an anode material for lithium ion batteries†

Guanhua Yang,[a] Zhixiong Yan,[a] Lisan Cui,[a] Yonghao Qu,[a] Qingyu Li,[*b] Xin Li,[a] Yiyan Wang[a] and Hongqiang Wang[*ac]

A Sn–Ni/graphite sheet composite is synthesized by a simple electroless plating method as an anode material for lithium ion batteries (LIBs). The microstructure and electrochemical properties of the composite are characterized by field emission scanning electron microscopy (FE-SEM), transmission electron microscopy (TEM), cyclic voltammetry (CV), and AC impedance spectroscopy. The results show that the as-prepared composite has Sn–Ni nanoparticles around 100 nm in size, where metallic Ni acts as an "anchor" to fix metallic Sn. The reunion phenomenon of Sn is alleviated by adding metallic Ni between the metallic Sn and graphite sheets. The Sn–Ni/graphite sheet electrode exhibits a good rate performance with a capability of 637.4, 586.3, 466.7, 371.5, 273.6, 165.3 and 97.3 mA h g^{-1} at a current density of 0.1, 0.2, 0.5, 1.0, 2.0, 5.0 and 10 A g^{-1}, respectively. The good electrical conductivity of Ni, high specific capacity of Sn and excellent cycling capability of the graphite sheets have a synergistic effect and are the main reasons behind the superior electrochemical performance. Furthermore, the as-prepared composite exhibits excellent lithium storage capacity and the reversible capacity increased as the cycle number increased.

Received 5th March 2018
Accepted 5th April 2018

DOI: 10.1039/c8ra01940a

rsc.li/rsc-advances

1. Introduction

Due to their high energy density, environmental friendliness and the absence of memory effects, lithium ion batteries (LIBs) have been widely used in portable electronic products (such as laptops, mobile phones, digital cameras, *etc.*), and have huge potential in the fields of electric and hybrid vehicles.[1–5] With the development of society and the progress of technology, the demand for high-performance batteries is urgently increasing.[6,7] Meanwhile, the anode materials of LIBs have a significant influence on their electrochemical performance, especially in the development of high-performance batteries. At present, one commercially applied anode material in LIBs is graphite, which possesses the characteristics of low cost, excellent electron conductivity, long cycle life and capacity stability. However, the theoretical capacity of graphite is only 372 mA h g^{-1}, which can hardly meet the requirements of high-capacity LIBs.[8,9] In order to obtain high capacity anode materials, numerous efforts are being made to find alternative materials to replace current commercial carbon for new LIBs.[10–15]

Among all the alternative materials, Sn metal is a promising non-carbon anode material with high theoretical capacity (994 mA h g^{-1}) and a low-voltage lithium-ion de-intercalation platform.[3,16] However, its significant volume expansion (200–300%) during cycles results in a reduction in specific capacity and cycle performance degradation, which limits its large-scale application in LIBs.[17–20] A typical strategy to overcome these shortcomings is to introduce an active or inert element that acts as a "buffer" to accommodate the large volume change during cycling. Researchers have shown that dispersing a Sn-based material in a carbon matrix is an effective way to form a stable Sn alloy or composite material to mitigate the volume effects of Sn and improve the cycling performance.[3,11,13,21,22]

Sn/C composite materials have already been obtained by various methods,[23–25] and most of them need high temperature treatment to ensure good conductivity. However, the melting point of Sn is only 232 °C and its dispersibility in composites is susceptible to heat treatment temperature. Under high temperature heat treatment, Sn particles tend to aggregate together into large particles,[23] which easily leads to powdering and falling of the electrode material during cycling, eventually resulting in the decrease of battery capacity and deterioration of the cycle performance.[26] Meanwhile, when the Sn/C composite material is treated with relatively low temperature, it has poor

[a]School of Chemical and Pharmaceutical Sciences, Guangxi Normal University, Guilin 541004, China
[b]Guangxi Key Laboratory of Low Carbon Energy Materials, Guangxi Normal University, Guilin 541004, China
[c]Hubei Key Laboratory for Processing and Application of Catalytic Materials, Huanggang Normal University, Huanggang 438000, China

† Electronic supplementary information (ESI) available. See DOI: 10.1039/c8ra01940a

electrical conductivity. Moreover, the connection between the Sn particles and the carbon is loose, which is not conducive to improving the electrochemical performance. In order to improve the conductivity of the composite material and inhibit the aggregation of metallic Sn at high heat treatment temperature, metallic Ni was introduced into the composite material.[27–29] Since nickel is a metal with good conductivity and its melting point is as high as 1453 °C, it can improve the electrical conductivity of the composite material and increase thermal tolerance.[17,30] Renzong Hu *et al.* prepared a Sn–C–Ni composite thin film by electron beam evaporation, which exhibited good capacity retention and a high rate capability.[22] B. D. Polat *et al.* prepared a Ni–Sn–C multilayered composite thin film by electron beam deposition, in which the interactions among Ni, Sn, and C atoms were enhanced and the electrode demonstrated good capacity performance.[31] Although Ni–Sn–C composite thin films with good electrochemical performance have been obtained, most methods used are not conducive to large-scale production due to the use of special equipment. For this reason, the facile synthesis of Sn–Ni–C multilayered anode materials with high capacity and long cycle life remains a challenge.

In this work, we use graphite sheets as the buffering/conducting matrix for Sn owing to their flexibility, mechanical strength, and electrical conductivity and propose a simple new strategy to prepare a Sn–Ni/graphite sheet composite material by electroless plating.[32] Metallic Ni in the composite material acts as a bridge connecting the graphite sheets and metallic Sn, preventing the aggregation of Sn at high heat treatment temperature. Meanwhile, Ni can improve the non-wetting properties between the metallic Sn and the non-metallic graphite sheets. Ni acts as an "anchor" in the as-prepared composite and limits the aggregation of Sn in a certain area, which is conducive to inhibiting metallic Sn reunion and improving the cycling performance of Sn. The enhanced electrochemical performance of the Sn–Ni/graphite sheets composite as an anode and the related mechanism are reported herein.

2. Experimental

2.1 Preparation of Sn–Ni/graphite sheet composite material

2.1.1 Preparation of oxidized graphite sheets. The oxidized graphite sheets were prepared by modified Hummer's method.[33,34] A certain amount of flake graphite powder, $NaNO_3$ and 98 wt% H_2SO_4 were mixed and vigorously stirred at 0 °C for 10 min in a three neck round bottom flask. Then a certain amount of $KMnO_4$ was added gradually to the above solution and reacted at 35 °C for 2 h. Right after the reaction was complete, 80 °C deionized water and 10 wt% H_2O_2 aqueous solution (with a volume ratio of 8 : 3) were added to the suspension and reacted at 90 °C for another 10 h. After cooling to room temperature, the black products were filtered and washed with a certain volume of 10 wt% HCl aqueous solution. Oxidized graphite sheets were obtained after washing with deionized water and drying.

2.1.2 Pre-treatment of graphite sheet surfaces. The electroless nickel plating consists of three basic processes: sensitization, activation and electroless plating. In this work, the graphite sheets were activated by a modified electroless plating method[35] in a solution containing 0.2 g L^{-1} $PdCl_2$ and 2.5 mL L^{-1} HCl for 30 min at room temperature. Pd catalytic nuclei can promote deposition of metallic Ni on the surface of oxidized graphite sheets.[36,37] A certain amount of $NaH_2PO_2 \cdot H_2O$ was then added slowly to the above solution and reacted for 30 min at room temperature. The chemical composition of the activation bath is shown in Table S1.†

2.1.3 Preparation of Ni/graphite sheet substrate. After activation, graphite sheets were introduced into the electroless bath containing nickel sulphate as the Ni^{2+} source and sodium hypophosphite as the reducing agent. In order to prevent nickel ion precipitation, Ni^{2+} ions must be complexed with a stronger complexing agent than water. Here we used citric acid, sodium acetate, and ammonium acetate as complexing agents. Table S2† shows the composition of the solutions used in the electroless nickel plating process. The aqueous solution was stirred by a magnetic stirrer for 1 h at 85 °C and its pH was controlled in the range 4.5–4.8. The Ni/graphite sheet substrate was obtained after repeatedly washing with deionized water and drying.

2.1.4 Preparation of Sn–Ni/graphite sheet composite material. After the electroless nickel plating process, the Ni/graphite sheet substrate was introduced into the electroless bath containing stannous chloride as the Sn^{2+} source and sodium hypophosphite as the reducing agent. Stannous chloride was dissolved in hydrochloric acid, and thiourea was used as a complexing agent. Table S3† gives the composition of the solutions used in the electroless tin plating process. The aqueous solution was stirred by a magnetic stirrer for 1 h at 80 °C and its pH was controlled in the range 2.0–5.0. After this, the composite material was obtained after repeatedly washing with deionized water and drying. As a comparison experiment, a Sn/graphite sheet composite material was synthesized by the electroless tin plating method using the same chemical compositions in Table S3.† In order to improve the crystallinity of the materials and make the oxidized graphite sheets reduce to graphite sheets, all of the resultant black precipitate was dried at 80 °C under vacuum, followed by heating in a tube furnace under high-purity Ar at 600 °C for 2 h.

2.2 Material characterization

The microstructure of the samples was characterized by field emission scanning electron microscopy (FESEM, Philips, FEI Quanta 200 FEG) and transmission electron microscopy (TEM, Tokyo, Japan, JEOL 2100F). The composition of the sample was analyzed by an energy dispersive spectroscope (EDS, INCA) attached to the SEM. Infrared spectra were recorded on a PE (Spot-light 3000) Fourier transform infrared (FTIR) spectrometer using the KBr disk technique to investigate the different functional groups in the powders before and after annealing. Raman spectroscopy (Spex Raman Log 1403) was employed to verify chemical bonding characteristics of carbon. Thermogravimetric analysis TG-DSC (SETARAM, LABSYS evo) was carried out in the temperature range 30 to 1000 °C at a scanning rate of 10 °C min^{-1} in air.

2.3 Electrochemical measurements

The electrochemical properties of the samples were tested using CR2032 coin-type half-cells, which were assembled in an argon-filled glove box with Li metal foil (Aldrich, USA) as the counter electrode. The working electrodes were prepared by coating homogeneous slurry on a copper foil. The slurry was composed of 85 wt% of active material, 10 wt% of conductivity agent (acetylene black), and 5 wt% of binder (polyvinylidene fluoride, PVDF). Then the electrodes were dried at 80 °C in a vacuum oven for 12 h and pressed to enhance the contact between the active material and the conductive carbons. During the preparation of the electrode, the mass loading of active material in the electrodes is about ~0.6 mg cm^{-2}. The electrolyte was composed of 1 M $LiPF_6$ and a mixture of ethylene carbonate (EC)/diethyl carbonate (DEC) 1 : 1 (vol%). Discharge–charge cycling tests were carried out at room temperature with a LAND test system, in the voltage range 0.01 V to 3.0 V (*vs.* Li/Li^+). Electrochemical impedance spectroscopy (EIS) was carried out in the frequency range 100 kHz to 10 mHz, and cyclic voltammograms (CVs) were measured with a scan rate of 0.1 mV s^{-1} in a potential range 1.0 mV to 3.0 V. Both EIS and CV tests were carried out on the IM6 electrochemical workstation (Zahner, Germany) at room temperature.

3. Results and discussion

3.1 The microstructure the of graphite sheets

As shown in Fig. 1a, flake graphite with neat edges is densely stacked together and the particle size distribution of flake graphite is in the range 4–10 μm. After the oxidation process, unlike flake graphite, oxidized graphite sheets exhibit a thin layered structure and only loosely connect with each other as shown in Fig. 1b, which suggests that the oxidation process promotes the stripping of flake graphite. The graphite sheets are further explored by FT-IR to evaluate their oxidation degree (Fig. S1†). The band of oxidized graphite sheets around 3150 cm^{-1} could be attributed to the stretching vibration of C–OH and –OH, which is shifted compared to the absorption peak of flake graphite (3437 cm^{-1}). The absorption peak at around 1733 cm^{-1} is mainly due to the C=O stretching vibration of carboxyl and carbonyl groups on the oxidized graphite sheets. The peak at approximately 1600 cm^{-1} is the characteristic O–H bending vibration of the water molecules, and the one near 1570 cm^{-1} is attributed to C=C bending vibrations.[38] FT-IR results show that the oxidation process can increase the number of oxygen containing groups on the surface of the layers. Moreover, Raman spectra (Fig. S2†) show that both flake graphite and oxidized graphite sheets show characteristic peaks of carbonaceous materials at around 1350 cm^{-1} (D band) and 1590 cm^{-1} (G band). The G and D bands are associated with the ordered sp^2 carbon and disordered effects and edge carbons, respectively. The ratio of I_D/I_G is used to measure the disorder in carbonaceous materials. It is obvious that the I_D/I_G value of oxidized graphite sheets (1.13) is greater than that of flake graphite (0.34), implying that homemade graphite sheets become more disordered after functionalization.[18] The graphitization of flake graphite decreases after activation, which is likely due to the more wavy or curly structure in oxidized graphite sheets. The Raman results are consistent with SEM and FT-IR. Thus, more oxygen containing groups are added on graphite sheets by the modified Hummer's method and the synthetic sandwich structure of graphite sheets can offer many attachment sites at the gaps and limit the reaction in a certain region.

3.2 The microstructure of the as-prepared Sn–Ni/graphite sheet composite material

Fig. 2a and b show SEM images of the electroless plated Sn/graphite sheet composite before and after sintering, respectively. In Fig. 2a, no particle is observed on the surface of graphite sheets, indicating that Sn particles do not reunite before heat treatment. However, since the melting point of Sn is only 232 °C, it is easy for Sn to transform into a molten state and gradually blend together under high temperature treatment. Then, molten Sn would reunite into particles when cooled, as shown in Fig. 2b. The size of the Sn particles is about 230 nm, as given in the inset. It indicates that Sn aggregates into large particles on the surface of the graphite sheets after sintering at 600 °C. Fig. 2c displays the electroless Ni/graphite sheet samples before sintering. It can be seen that small floccules

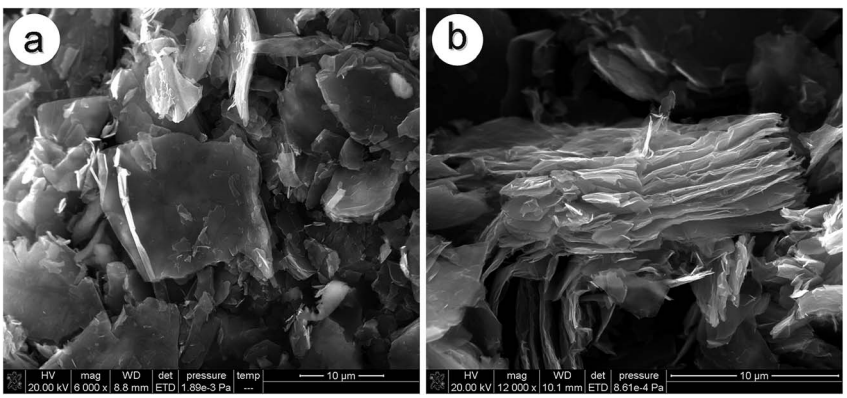

Fig. 1 SEM images of flake graphite (a) and oxidized graphite sheets (b).

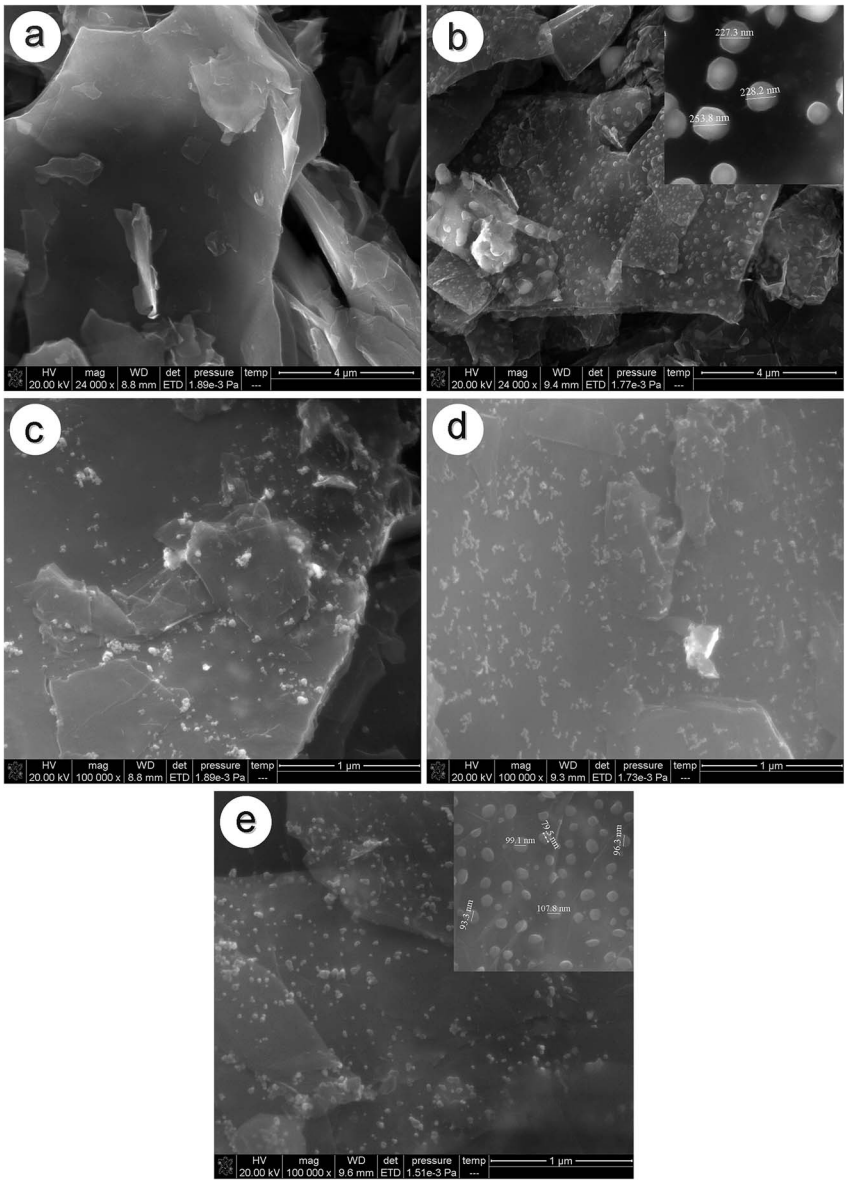

Fig. 2 SEM images of the Sn/graphite sheet sample before sintering (a) and after sintering at 600 °C (b), the Ni/graphite sheet sample before sintering (c), and the Sn–Ni/graphite sheet sample before sintering (d) and after sintering at 600 °C (e).

disperse uniformly on the graphite sheets. Fig. 2d and e are SEM images of electroless plated Sn–Ni/graphite sheet composites before and after sintering, respectively. Fig. 2d shows that the sample has similar flocculent particles on the surface of the graphite sheets before sintering. Compared to Fig. 2c, the flocculent particles are smaller and distribute more evenly, indicating that the agglomeration of particles is effectively alleviated. This may be because the metallic Ni acts as the active site, which can prevent the particles contacting with each other. Fig. 2e shows that a lot of small spherical particles disperse evenly on the matrix of graphite sheets. Compared to the particles in Fig. 2b, the size of the particles in Fig. 2e is much smaller, with a diameter around 100 nm. This is because Ni has a high melting point, which makes metallic Sn withstand the heat treatment temperature of 600 °C without severe agglomeration. In addition, Ni particles can be used as attachment points for Sn, which means Sn effectively covers the surface of the Ni and is fixed in certain area. Thus, this special "anchor" structure of the Sn–Ni/graphite sheet sample can improve the heat treatment temperature of the composite material and effectively inhibit the accumulation of metallic Sn.

In order to investigate the microstructure of the Sn–Ni/graphite sheet composite after sintering at 600 °C, TEM observations were carried out. They revealed clearly that the composite is composed of lots of similar core/shell nanoparticles, in which the Ni particles are dispersed inside and the Sn particles form a shell and cover the Ni particles.[22] The Sn–Ni particles uniformly attach to the graphite sheets, as shown in Fig. 3a. The selected area electron diffraction (SAED) pattern proves that the composite material is polycrystalline, shown as

an inset in Fig. 3a. These particles are Sn and Ni, which is consistent with the previous reports.[22,27] The enlarged image of the composite material in Fig. 3b also shows that Sn–Ni particles with a size of about 100 nm homogeneously disperse on the graphite sheets. It shows that the micro-sized Ni are fully wrapped by the metallic Sn and the shell thickness of Sn is about 70 nm. The enlarged image of the composite is shown as an inset in Fig. 3b, and further proves that the Sn particles cover the Ni particles, forming Sn–Ni particles. It is proven by the EDS (Fig. 3c) that the nano-composite mainly contains a homogeneous spatial distribution of C, O, Sn and Ni, and the content of each element is 40.8%, 15.5%, 31.4%, and 12.3%, respectively. It also verifies that the nickel metal and metallic tin were effectively deposited on the graphite sheet surface by electroless plating. The composite material contains some oxygen, which is because oxygen-containing groups are not completely removed at 600 °C. Fig. 3d shows the TGA curves of Ni/graphite sheets and Sn–Ni/graphite sheets in air in the temperature range of room temperature to 1000 °C with a heating rate of 10 °C min^{-1}. The first mass loss in the region 30–100 °C is ascribed to the release of adsorbed water and the second mass loss in the region 100–600 °C may be correlated to the removal of the graphite sheets. Therefore, the weight fraction of the graphite sheets is about 48% by weight. From Fig. 3d, it can be estimated that the amount of NiO and SnO_2 in the Sn–Ni/graphite sheets is about 37.7% and 10.8%, respectively. Based on the weight ratio of NiO and SnO_2, the loading ratio of Ni and Sn by weight was calculated to be 29.6% and 8.5%, respectively, which is consistent with the EDS results.

The deduced formation mechanism of the Sn–Ni/graphite sheet composite is presented schematically in Scheme 1. Firstly, homemade graphite sheets with a layered structure are prepared by a modified Hummer's method and are expected to increase the surface area of the composite material and alleviate the volume effect of the metallic Sn. After the graphite sheets have been activated, Pd active sites are distributed evenly on the graphite sheets. Subsequently, metallic Ni is deposited on the surface of the pretreatment graphite sheets by electroless plating, then metallic Sn is deposited on the surface of the Ni. The volume effect of the Sn in the as-prepared composite material is constrained by the interaction between the Ni and the graphite sheets. The metallic Ni acts as attachment sites, which makes the Sn gather around the metallic Ni. The Ni tightly connects the graphite sheets and the metallic Sn, and the high melting point of Ni improves the heat resistance of the composite material and prevents the melting Sn from

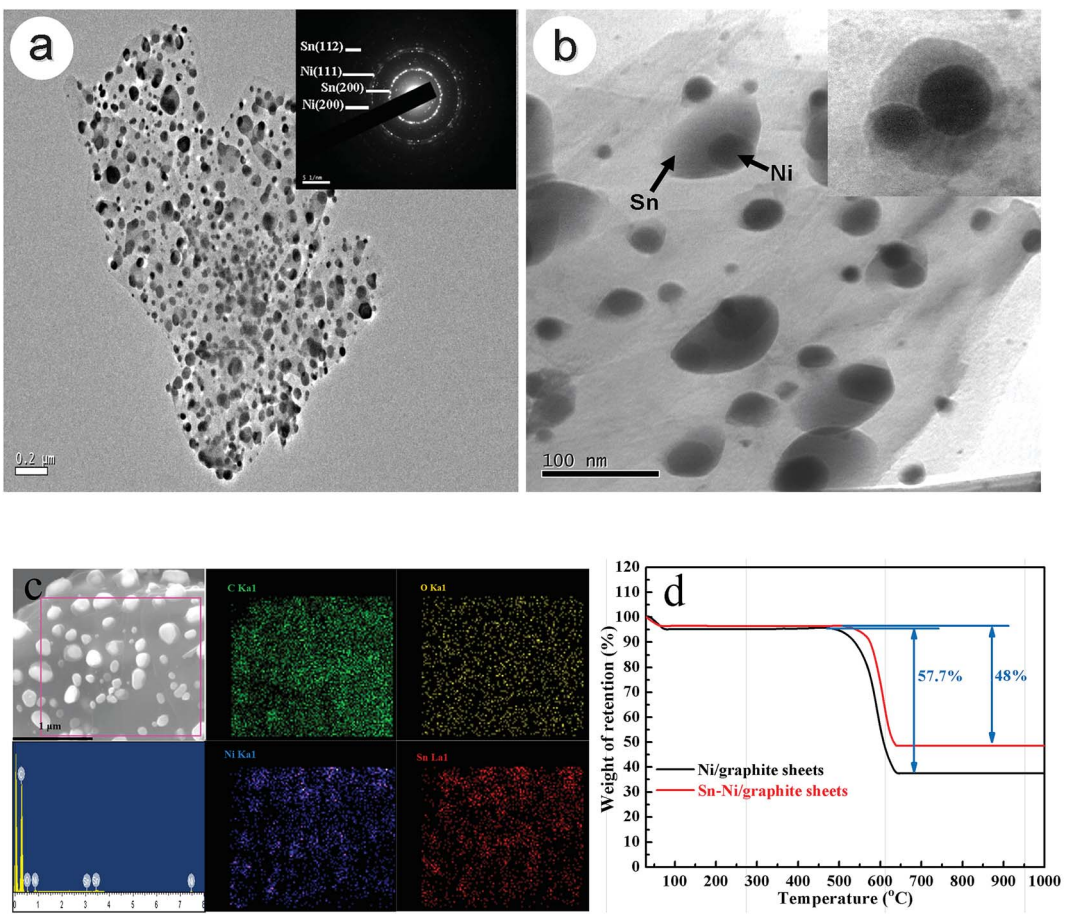

Fig. 3 TEM images of the Sn–Ni/graphite sheet sample with the corresponding SAED patterns (inset) (a) and the nano-phases dispersed in the Sn–Ni/graphite sheets (b), EDS spectrogram of the Sn–Ni/graphite sheet sample and elemental distribution for C, O, Ni, Sn (c), and TGA curves of Ni/graphite sheets and Sn–Ni/graphite sheets (d).

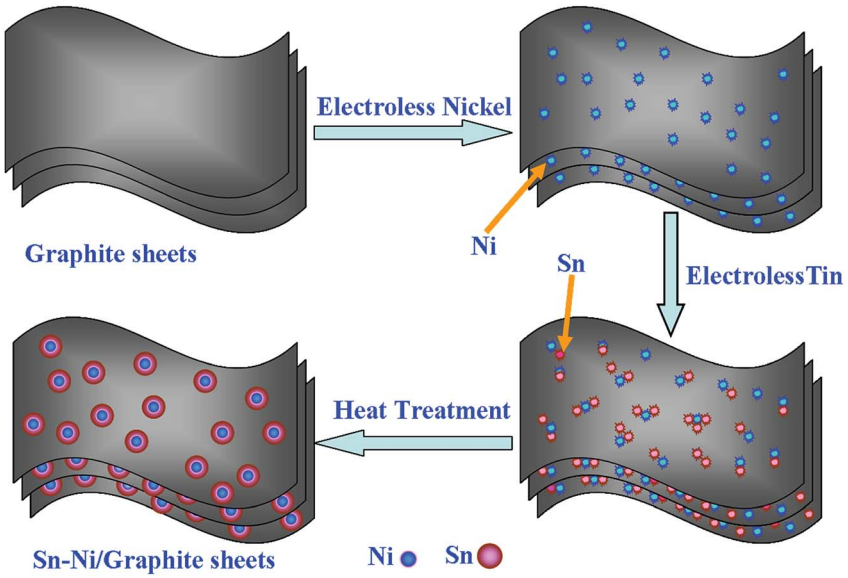

Scheme 1 The formation mechanism of the Sn–Ni/graphite sheet composite material.

aggregating under high heat treatment temperature. The good wettability between Sn and Ni in the as-prepared composite may help to reduce the impedance value of the composite. The good electrical conductivity of Ni, high specific capacity of Sn and excellent cycling capability of graphite sheets will be synergistically conducive in improving the electrochemical properties of the Sn–Ni/graphite sheet composite.

3.3 Electrochemical properties of the Sn–Ni/graphite sheet composite

The CV curves of the first three cycles for the Sn–Ni/graphite sheets, Sn/graphite sheets and Ni/graphite sheets at a scan rate of 0.1 mV s^{-1} in the range 1.0 mV to 3.0 V are shown in Fig. 4a–c, respectively. As shown in Fig. 4, all the cells display a similar broad peak within the range of 0.30–0.70 V during the first reduction process which then disappears in the subsequent two cycles, which is in accordance with the decomposition of the electrolyte and the subsequent formation of solid electrolyte interphase (SEI) films. In Fig. 4a, there is no obvious peak near 0.8 V in the cathodic process in the first cycle. This phenomenon is mainly due to the poor wetness of the electrolyte on the active substance, which impedes the embedding process of the lithium ion into Sn. A sharp peak appears near 0.01 V, which is attributed to the insertion of Li^+ into the graphite layers to form Li_xC. In the anodic process, the peak at around 0.25 V corresponds to the process of lithium ion extraction from the graphite sheets. On the next two cycles, it can be seen that two peaks appear at about 0.75 and 0.25 V in the cathodic process, which are consistent with the reaction of Li with Sn. The subsequent anodic curves show two peaks at approximately 0.80 and 0.15 V, which are attributed to the extraction of Li from Li_xSn and the graphite sheets, respectively. The CV curves of the Sn/graphite sheets are displayed in Fig. 4b. The Sn/graphite sheets show similar peaks at about 0.80, 0.25, 0.01 V in the cathodic process, which can be ascribed to the formation of the Li_xSn alloy and Li^+ insertion into the graphite sheets. The peaks at approximately 0.85 and 0.25 V represent Li^+ deinsertion from the Li_xSn alloy and Li^+ extraction from the graphite sheets, respectively. Comparing Fig. 4a and b, the introduction of metallic nickel not only maintained the behavior of insertion/deinsertion from the Li_xSn alloy, but also improved the reversibility of the reaction in the cyclic voltammetry, especially in the second and third cycle. As shown in Fig. 4c, the Ni/graphite sheets composite material shows better reversibility than the graphite sheets composite material (see Fig. S3 in the ESI †), agreeing well that the introduction of nickel can improve the electrochemical reversibility of the Sn–Ni/graphite sheets. These results further indicate that nickel and tin have been successfully deposited on the graphite sheets by electroless plating. It confirms that lithium ions can not only be inserted into and extracted from the graphite layer, but also react with tin. Additionally, it verifies that nickel can enhance the electrochemical reversibility of the Sn–Ni/graphite sheets.

Fig. 5 shows the discharge–charge curves of the Sn–Ni/graphite sheets, Sn/graphite sheets and Ni/graphite sheets electrodes at the 1st, 2nd, 10th cycle between 0.01–3.0 V with a current density of 0.1 A g^{-1}. For the Sn–Ni/graphite sheets in Fig. 4a, the charge and discharge curves show a wide potential plateau at 0.25 to 0.01 V, corresponding to the process of lithium ion intercalation and deintercalation from the graphite sheets. The steep profile of 0.85 to 0.25 V is related to the processes of the lithium ions being embedded into the Sn and extracted from Li_xSn. The above results are consistent with the results of the CVs in Fig. 4a. The Sn–Ni/graphite sheets show discharge and charge capacities during the first cycle of 1208.9 and 633.4 mA h g^{-1}, respectively, and the coulombic efficiency in the first charge/discharge cycle is 52.4%. This large irreversible capacity during the initial cycle may be caused by the formation of solid electrolyte interphase (SEI) or associated with the trapping of Li ions in the defects of the composite material. However, in the

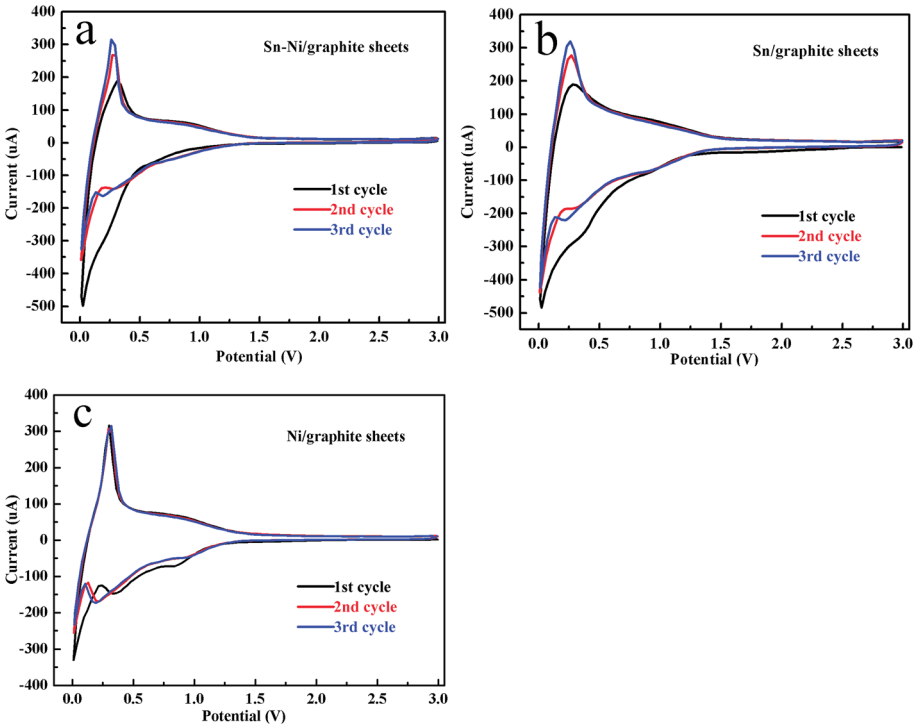

Fig. 4 The first three CV curves of the Sn–Ni/graphite sheets (a), the Sn/graphite sheets (b) and the Ni/graphite sheets (c) with a scan rate of 0.1 mV s^{-1} between 1.0 mV and 3.0 V.

subsequent charge–discharge cycles, the coulombic efficiency of the 10th cycle increases to 98.7% (the 10th cycle discharge and charge capacities are 633.8 and 642.2 mA h g^{-1}), indicating that the capacities of the composite material electrode are highly reversible and that the electrode tends to be stable. For comparison, the Sn/graphite sheets exhibit initial discharge and charge capacities of 958.0 and 530.7 mA h g^{-1}, respectively. The Ni/graphite sheets display initial discharge and charge capacity of

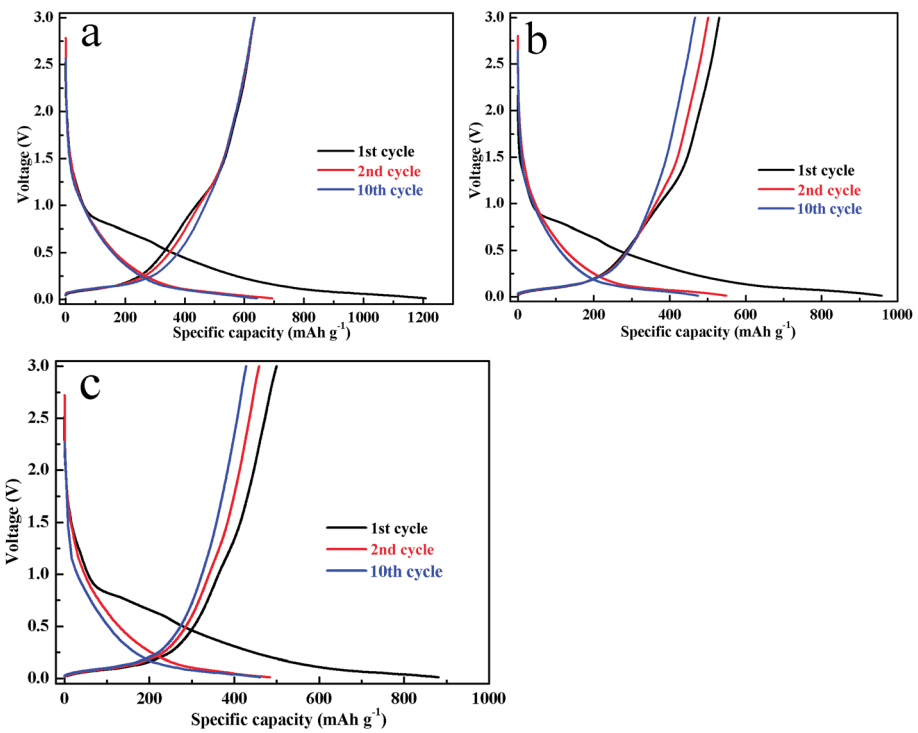

Fig. 5 The 1st, 2nd and 10th discharge–charge curves of the Sn–Ni/graphite sheets (a), the Sn/graphite sheets (b) and the Ni/graphite sheets (c).

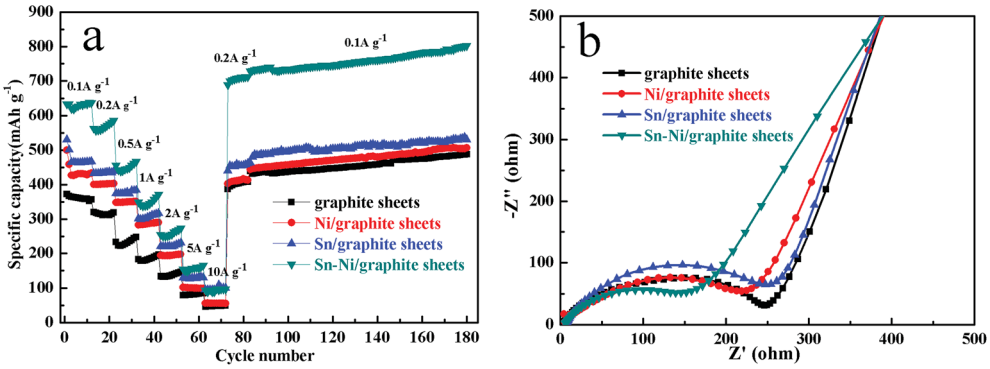

Fig. 6 The rate capability and cycling performance of the graphite sheets, Ni/graphite sheets, Sn/graphite sheets and Sn–Ni/graphite sheets (a), and the electrochemical impedance spectra of the graphite sheets, Ni/graphite sheets, Sn/graphite sheets and Sn–Ni/graphite sheets (b).

881.1 and 499.9 mA h g^{-1}, respectively. In subsequent cycles, the Sn/graphite sheets and Ni/graphite sheets 10th cycle charge capacities are 466.9 and 428.4 mA h g^{-1}, respectively. Therefore, the Sn–Ni/graphite sheets show higher capacity than the other samples (the 1st, 2nd and 10th discharge–charge capacities are shown in Fig. S4†), which may be due to the introduction of metallic Ni alleviating the volume effect of Sn, thereby increasing the reversible capacity of the composite material.

In order to further investigate the electrochemical performance of the graphite sheets, Sn/graphite sheets, Ni/graphite sheets and Sn–Ni/graphite sheet electrodes, rate performance and continuous cycling tests of different electrodes were carried out, and the results are shown in Fig. 6a. All of the cells are first activated by cycling at current densities of 0.025 A g^{-1} and 0.05 A g^{-1}, respectively. Then the cells are cycled at current densities of 0.1 A g^{-1} to 10 A g^{-1}, returned to 0.2 A g^{-1} and continuously cycled at a current density of 0.1 A g^{-1}. It can be seen that the capacity decreases with an increase in rate, and the capacity increases again after the rate is reversed back to 0.2 A g^{-1}. Furthermore, all the electrodes show excellent rate capability at each rate. Obviously, compared to the other electrodes, the Sn–Ni/graphite sheets electrode displays the most excellent lithium storage capacity at each current density. With increasing current density of 0.1, 0.2, 0.5, 1.0, 2.0, 5.0 and 10 A g^{-1}, the capacities at the end of each rate were measured as 637.4, 586.3, 466.7, 371.5, 273.6, 165.3 and 97.3 mA h g^{-1}, respectively. When the current density returned to 0.2 A g^{-1}, the Sn–Ni/graphite sheet electrode still displayed an impressive specific capacity of 712.3 mA h g^{-1}, higher than the capacity of 586.3 mA h g^{-1} at 0.2 A g^{-1} displayed at the beginning. This could be attributed to the metallic nickel, metallic tin and graphite sheets synergistically increasing the lithium storage capacity by expanding the ion transmission channels facilitating lithium ions to transfer into deeper regions, so the electrode could be activated during the cycle. After cycling at each rate, the electrodes continued to cycle for another 100 cycles at 0.1 A g^{-1}, and the capacity of the Sn–Ni/graphite sheet electrode retained a capacity as high as 802.4 mA h g^{-1}. For comparison, the capacities at the end of each rate and continuous cycling test for the graphite sheets, Sn/graphite sheets, and Ni/graphite sheets are also provided in Table S4,† which reveal that the introduction of metallic tin or metallic nickel can improve the rate performance and cycling performance of the composites. The above results prove that the as-prepared Sn–Ni/graphite sheets possess high rate capability and good cycling performance for potential application in lithium ion batteries.

Electrochemical impedance spectra (EIS) measurements were recorded for the graphite sheets, Sn/graphite sheets, Ni/graphite sheets and Sn–Ni/graphite sheets after 3 cycles to further expound the electrochemical kinetics. As shown in Fig. 6b, both of the Nyquist plots display a semicircle in the high frequency region and a sloping straight line in the low frequency region. The semicircle implies the charge-transfer process between the active material and the electrolyte (R_{ct}).[31] Compared to the graphite sheets and the Sn/graphite sheets, the impedance value of the Ni/graphite sheets and the Sn–Ni/graphite sheets is much smaller in the high-medium frequency region. Obviously, the resistance of the Sn–Ni/graphite sheets is the smallest because of the introduction of nickel, which could be attributed to the high conductivity of Ni and the synergistic effects between each component effectively decreasing the resistance of the composites. The straight line indicates the typical characteristics of the Warburg impedance Z_w, generally representing the presence of Li^+ diffusion in the coatings of the active material.[39,40] It can be seen that the different electrodes exhibit different slopes, suggesting lithium ions have different diffusion coefficients in the graphite sheets, Sn/graphite sheets, Ni/graphite sheets and Sn–Ni/graphite sheets.[41] The curves of all the as-prepared materials have a similar slope, suggesting all of them possess good ion diffusion performance. The results above show that the introduction of nickel can reduce the impedance of the composites and remarkably enhance the electron and Li^+ ion transport performance of the Sn–Ni/graphite sheets in LIBs.

4. Conclusions

In summary, Sn–Ni/graphite sheet materials are successfully synthesized by a simple electroless plating method followed by heat-treatment. The structure design not only integrates the excellent conductivity of Ni and graphite sheets, but also integrates the buffering effects of Ni and graphite sheets, which is

proven to be an effective way to improve the electrochemical performance of anode materials for LIBs. The results show that the rate performance and the cycling performance of the composite are improved significantly and a capacity of 802.4 mA h g^{-1} is obtained after rate cycling and continued cycling for another 100 cycles. Facile synthesis of the Sn–Ni/graphite sheets by electroless plating provides a strategy for improving the electrochemical performance of anode materials for Li-ion batteries.

Conflicts of interest

There are no conflicts to declare.

Acknowledgements

This research was supported by the Hubei Province Key Science and Technology Support Program (No. 2015BCE072), the Outstanding Young Science and Technology Innovation Team Program of Hubei Province Colleges and Universities (No. T201514), the Scientific Research and Technological Development Program of Guilin (2016010502-2), the "1020" Innovation-Driven Plan of Guilin (20160211), and the Department of Education of Guangxi Zhuang Autonomous Region (A-2905-14-000008).

References

1 K. Cao, P. Li, Y. Zhang, T. Chen, X. Wang, S. Zhang, J. Liu and H. Wang, *Nano Energy*, 2017, **40**, 187–194.
2 J. Chen and K. Yano, *ACS Appl. Mater. Interfaces*, 2013, **5**, 7682–7687.
3 Y. Cheng, Z. Yi, C. Wang, Y. Wu and L. Wang, *Chem. Eng. J.*, 2017, **330**, 1035–1043.
4 J. Leng, Z. Wang, X. Li, H. Guo, H. Li, K. Shih, G. Yan and J. Wang, *J. Mater. Chem. A*, 2017, **5**, 14996–15001.
5 T. Li, X. Li, Z. Wang, H. Guo, Y. Li and J. Wang, *J. Mater. Chem. A*, 2017, **5**, 13469–13474.
6 W. Yue, S. Yang, Y. Ren and X. Yang, *Electrochim. Acta*, 2013, **92**, 412–420.
7 D. B. Polat, J. Lu, A. Abouimrane, O. Keles and K. Amine, *ACS Appl. Mater. Interfaces*, 2014, **6**, 10877–10885.
8 J. Qin, X. Zhang, N. Zhao, C. Shi, E. Liu, J. Li and C. He, *RSC Adv.*, 2014, **4**, 49247–49256.
9 H. Liu, R. Hu, W. Sun, M. Zeng, J. Liu, L. Yang and M. Zhu, *J. Power Sources*, 2013, **242**, 114–121.
10 P. Wu, H. Wang, Y. Tang, Y. Zhou and T. Lu, *ACS Appl. Mater. Interfaces*, 2014, **6**, 3546–3552.
11 X. Shi, H. Song, A. Li, X. Chen, J. Zhou and Z. Ma, *J. Mater. Chem. A*, 2017, **5**, 5873–5879.
12 Z. Wang, S. Luo, F. Chen, D. Wang, Y. Liu, X. Qi, C. Shi and N. Zhao, *RSC Adv.*, 2016, **6**, 54718–54726.
13 K. Wang, Y. Huang, D. Wang, Y. Zhao, M. Wang, X. Chen and H. Wu, *RSC Adv.*, 2016, **6**, 23260–23264.
14 Z. Yan, Q. Hu, G. Yan, H. Li, K. Shih, Z. Yang, X. Li, Z. Wang and J. Wang, *Chem. Eng. J.*, 2017, **321**, 495–501.
15 J. Wang, G. Zhang, Z. Liu, H. Li, Y. Liu, Z. Wang, X. Li, K. Shih and L. Mai, *Nano Energy*, 2018, **44**, 272–278.
16 Q.-c. Pan, Y.-g. Huang, H.-q. Wang, G.-h. Yang, L.-c. Wang, J. Chen, Y.-h. Zan and Q.-y. Li, *Electrochim. Acta*, 2016, **197**, 50–57.
17 D. Jiang, X. Ma and Y. Fu, *J. Appl. Electrochem.*, 2012, **42**, 555–559.
18 B. Lee, S. C. Han, M. Oh, M. S. Lah, K.-S. Sohn and M. Pyo, *Electrochim. Acta*, 2013, **113**, 149–155.
19 M. P. B. Glazer, J. Wang, J. Cho, J. D. Almer, J. S. Okasinski, P. V. Braun and D. C. Dunand, *J. Power Sources*, 2017, **367**, 80–89.
20 P. Dou, Z. Cao, J. Zheng, C. Wang and X. Xu, *J. Alloys Compd.*, 2016, **685**, 690–698.
21 H. Shi, A. Zhang, X. Zhang, H. Yin, S. Wang, Y. Tang, Y. Zhou and P. Wu, *Nanoscale*, 2018, **10**, 4962–4968.
22 R. Hu, H. Liu, M. Zeng, H. Wang and M. Zhu, *J. Mater. Chem.*, 2011, **21**, 4629–4635.
23 D. Wang, X. Li, J. Yang, J. Wang, D. Geng, R. Li, M. Cai, T. K. Sham and X. Sun, *Phys. Chem. Chem. Phys.*, 2013, **15**, 3535–3542.
24 J. Wang, D. Li, X. Fan, L. Gou, J. Wang, Y. Li, X. Lu and Q. Li, *J. Alloys Compd.*, 2012, **516**, 33–37.
25 S. Liang, X. Zhu, P. Lian, W. Yang and H. Wang, *J. Solid State Chem.*, 2011, **184**, 1400–1404.
26 Z. Wen, S. Cui, H. Kim, S. Mao, K. Yu, G. Lu, H. Pu, O. Mao and J. Chen, *J. Mater. Chem.*, 2012, **22**, 3300–3306.
27 H. Guo, H. Zhao and X. Jia, *Electrochem. Commun.*, 2007, **9**, 2207–2211.
28 J. Chen, S. J. Bull, S. Roy, A. Kapoor, H. Mukaibo, H. Nara, T. Momma, T. Osaka and Y. Shacham-Diamand, *Tribol. Int.*, 2009, **42**, 779–791.
29 L. Ouyang, J. Huang, H. Wang, J. Liu and M. Zhu, *Mater. Chem. Phys.*, 2017, **200**, 164–178.
30 S.-W. Woo, N. Okada, M. Kotobuki, K. Sasajima, H. Munakata, K. Kajihara and K. Kanamura, *Electrochim. Acta*, 2010, **55**, 8030–8035.
31 B. D. Polat, A. Abouimrane, N. Sezgin, O. Keles and K. Amine, *Electrochim. Acta*, 2014, **135**, 585–593.
32 J. Liang, Y. Zhao, L. Guo and L. Li, *ACS Appl. Mater. Interfaces*, 2012, **4**, 5742–5748.
33 H.-Q. Wang, G.-H. Yang, Y.-G. Huang, X.-H. Zhang, Z.-X. Yan and Q.-Y. Li, *Mater. Chem. Phys.*, 2015, **167**, 303–308.
34 H. Liu, J. Huang, X. Li, J. Liu, Y. Zhang and K. Du, *Phys. E*, 2012, **44**, 1931–1935.
35 L.-M. Ang, T. S. Andy Hor, G.-Q. Xu, C.-H. Tung, S. Zhao and J. L. S. Wang, *Chem. Mater.*, 1999, **11**, 2115–2118.
36 J. Li, M. Moskovits and T. L. Haslett, *Chem. Mater.*, 1998, **10**, 1963–1967.
37 J. Guerra and M. Herrero, *Nanoscale*, 2010, **2**, 1390–1400.
38 H. Liu, J. Huang, X. Li, J. Liu, Y. Zhang and K. Du, *Appl. Surf. Sci.*, 2012, **258**, 4917–4921.
39 J. Zhu, D. Wang, L. Wang, X. Lang and W. You, *Electrochim. Acta*, 2013, **91**, 323–329.
40 J.-Y. Lin, M.-H. Chou and Y.-C. Kuo, *J. Alloys Compd.*, 2014, **589**, 472–478.
41 P. Guo, H. Song and X. Chen, *Electrochem. Commun.*, 2009, **11**, 1320–1324.